



Energy Transfer in Color-Tunable Water-Dispersible Tb-Eu codoped CaF₂ Nanocrystals

Received 00th January 20xx,
Accepted 00th January 20xx

DOI: 10.1039/x0xx00000x

www.rsc.org/

M. Back,^{a*} R. Marin,^a M. Franceschin,^a N. Sfar Hancha,^a F. Enrichi,^{b,c} E. Trave,^a and S. Polizzi^{a,d}

The development of highly luminescent water-dispersible biocompatible nanoparticles is a hot topic in biomedical research. Here, we report about the study of the energy transfer process between Tb³⁺ and Eu³⁺ in calcium fluoride nanoparticles. Water-dispersible RE-doped nanoparticles were prepared by means of a simple synthesis route without the need of high temperature, pressure or additional surface functionalization. The structural and morphological properties were investigated by means of XRPD and TEM analysis. The optical analysis led information about both the RE ion site symmetry in the crystalline host and the Tb³⁺ and Eu³⁺ excited state lifetimes, whose remarkable duration is suitable for biosensing application. Concerning the energy transfer process, dipole-dipole interaction, with a donor-activator critical distance of about 13 Å, was identified as the most probable mechanism.

1. Introduction

Luminescent nanoparticles have attracted large interest in recent years because of the many applications where they are superior to their corresponding bulk phase, as for lamps, displays optoelectronics and photovoltaics or where nanometric size is required, as in surface coatings or biolabeling.¹⁻³ For the latter applications, biocompatibility, non-toxicity and water dispersibility are also of uttermost importance.

Luminescent biolabeling, through up- or down-conversion, may be obtained by organic dyes⁴ or quantum dots,^{5,6} but most of these materials suffer from a series of intrinsic limitations, such as photodegradation, cytotoxicity, small Stokes shift (overlapping of emission and absorption bands), broad emission band width. Lanthanide-doped inorganic nanoparticles are not subject to these drawbacks and at the same time show high luminescent quantum yield and long lifetime, allowing one to use time-resolved photoluminescence to increase the signal-to-noise ratio and thereby significantly improve biodetection.⁷ In such materials, the crystal structure of the inorganic host needs to be apt to accommodate the doped ions without introducing defects and to possess as low as possible a phonon energy, in order to minimize non-

radiative relaxation processes that cause luminescence quenching.

Fluorides, and in particular CaF₂, are considered among the best matrix for lanthanide ions because of their low phonon energy, high environmental and thermal stability, non-toxicity and bio-compatibility. The phonon energy of CaF₂ is almost 328 cm⁻¹, one of the lowest known.⁸

In order to be useful for bio-labeling applications, nanoparticles need, in addition, to be dispersible in water. Since as-prepared CaF₂ nanoparticles are usually not easily dispersible in water, strategies have been proposed to induce dispersibility by surface functionalization (cappant or chelating agents). Pedroni *et al.* obtained water-dispersible lanthanide-doped CaF₂ nanoparticles for up-conversion (Ln³⁺ = Er/Yb, Tm/Yb, Ho/Yb) using an oleate anion or a citrate anion as a capping agent in a hydrothermal synthesis.^{9,10} The latter anion was also used by Sasidharan *et al.* for down-converting CaF₂:Eu³⁺ nanoparticle, through a simple aqueous wet chemical route at room temperature.¹¹ More recently, Song *et al.* obtained down-converting CaF₂ nanoparticles (Ln³⁺ = Eu, Tb, Ce/Tb) using PVP as a coating ligand, which also demonstrated to act as a sensitizer for the Tb³⁺ ion.¹² Finally, Zhao *et al.* used micro-wave assisted solvothermal synthesis using adenosine 5'-triphosphate disodium salt (ATP) as a functionalization agent to obtain up-converting CaF₂:Yb³⁺/Er³⁺ nanocrystals.¹³

However, already in 2009 J. Wang *et al.* proposed a very facile co-precipitation method in methanol solution for obtaining water-dispersible CaF₂ nanocrystals, using no specific capping agent.¹⁴ The dispersibility was attributed to a large number of hydroxyl groups either chemically bonded or physically adsorbed to the surface and, possibly, to methanol

^a Dipartimento di Scienze Molecolari e Nanosistemi, Università Ca' Foscari Venezia, via Torino 155, 30172 Mestre - Venezia, Italy. E-mail: michele.back@unive.it

^b Veneto Nanotech, Laboratorio Nanofab, via delle Industrie 5, 30175 Marghera (Venezia), Italy

^c CNR-IFN Istituto di Fotonica e Nanotecnologie, CSMFO Lab., Via alla Cascata 56/C, 38123 Povo (Trento), Italy

^d Centro di Microscopia Elettronica "Giovanni Stevanato" via Torino 155, 30172 Venezia-Mestre, Italy

[†] Electronic Supplementary Information (ESI) available: [details of any supplementary information available should be included here]. See DOI: 10.1039/x0xx00000x

molecules acting as a ligand coordinating with lanthanide ions. On the other hand, hydroxyl groups are usually claimed to quench luminescence, so that the nevertheless high luminescent efficiency of this material suggests that the large majority of the lanthanide ions is protected inside the structure of the matrix and do not suffer from the influence of the deleterious luminescent quenching surface groups. The synthesis was used for obtaining down-converting materials using Eu³⁺ or Tb³⁺ dopants which display intense red and green luminescence under ultraviolet excitation, respectively.

In the present study we used the latter synthesis and explored the effect of co-doping with the two lanthanide ions. We demonstrate energy transfer from Tb³⁺ to Eu³⁺ ions with allows one to enhance luminescence and at the same time tune the colour of emission using different doping ratios and/or different excitation wavelength. Although the sensitization effect of Tb³⁺ ions on Eu³⁺ luminescence has been demonstrated in several systems,¹⁵⁻²¹ to the best of our knowledge the energy transfer between these two ions was not previously studied in CaF₂ nanocrystals. The only reported example of energy transfer in CaF₂:Eu,Tb is a “proof-of-concept” single sample described by Ritter *et al.* for non-water-dispersible particles (methanol) obtained using a much more complex synthesis,²² in a paper otherwise dedicated to separate doping with Eu³⁺ or Tb³⁺ ions and the physical mixture of differently doped nanoparticles, where energy transfer did not take place.

2. Experimental

2.1. Chemicals

CaCl₂ (93%), EuCl₃*6H₂O (99.9%), TbCl₃ (99.99%) and Methanol were purchased from Sigma-Aldrich while NH₄F (98%) and Ethanol from Fluka. All chemicals were used without further purification.

2.2. Synthesis of Tb-Eu codoped CaF₂ nanocrystals

Starting from a modification of the procedure reported in J. Wang *et al.*,¹⁴ in a typical synthesis 8 mmol of NH₄F were dissolved in 30 ml of anhydrous methanol at about 75°C, stirring the solution for 10 minutes (until the thermalization is reached and MeOH starts boiling). Another solution of 4 mmol of CaCl₂ and dopant salts in 5 ml of methanol was prepared and added dropwise to the ammonium fluoride solution. The reaction was protracted for 3 h stirring the solution at 75°C. Once cooled at room temperature, the product was collected by centrifugation at 12000 rpm for 40 min and washed twice with ethanol:water 5:1. Finally, the nanocrystals were stored in water at a concentration of 1 mg/mL. All samples were synthesized by means of the same procedure, with the variation of the Ca^{2+:}Tb^{3+:}Eu³⁺ content ratio by maintaining the total amount of 4 mmol. Samples are labelled as Tb_XEu_Y, where X and Y are atomic contents.

2.3. Characterization

In order to investigate the microstructure of the obtained nanocrystals by X-ray powder diffraction (XRPD), the solutions were dried overnight at 60°C. A Philips diffractometer with a PW1319 goniometer and Bragg-Brentano geometry, connected to a highly stabilized generator (40 kV), was used. The set-up included a focusing graphite monochromator and a proportional counter with a pulse-height discriminator. Nickel-filtered Cu K_α radiation and a step-by-step technique were employed (steps of 0.05 in 2θ), with collection times of 10 s per step.

Transmission Electron Microscope (TEM) images were taken at 300 keV using a JEOL 3010 instrument with an ultrahigh resolution (UHR) pole-piece (0.17 nm point resolution), equipped with a Gatan slow scan CCD camera (model 794). The powders were dispersed in isopropyl alcohol by means of sonication and then deposited onto a holey carbon film-coated copper grid.

Photoluminescence analysis (excitation, emission and lifetime measurements) were carried out using a Horiba-Jobin Yvon Fluorolog 3-21 spectrophotometer. The photoluminescence spectra were collected exciting the samples by means of a xenon arc lamp (450 W), selecting the excitation wavelength with a double Czerny-Turner monochromator. The excitation and emission spectra were recorded in 1 nm bandpass resolution. Time resolved photoluminescence measurements were carried out at room temperature (RT) under excitation at 355 nm using an Ekspla NT 342/3/UVE/AW Q-switched Nd:YAG laser. The detection system consists of an iHR300 single grating monochromator coupled to an R928 Hamamatsu photomultiplier tube. All spectra were recorded at RT under the same conditions.

3. Results and discussion

3.1. Structure and morphology

As shown in Fig. 1(a), the *Fm-3m* fluorite-type CaF₂ cubic phase (PDF 35-0816) was recognized for all of the synthesized samples. The absence of other peaks in the XRPD patterns confirms the good success of the synthesis and the homogeneous inclusion of the Eu³⁺ and Tb³⁺ ions in the structure. Although the ionic radius of both doping ions is smaller than the Ca²⁺ one, the magnification of the (111) reflection (Fig. 1(a) right-hand side) evidences a peak shift to lower angles with increasing rare-earth content, indicating a cell edge increase. Rietveld refinement allowed us to calculate the cell edge and the corresponding cell volume, quantitatively confirming the cell edge enlargement with increasing lanthanide content (see Fig. 1(b)). As suggested by F. Wang *et al.*,²³ this increase of lattice parameters may be ascribed to the formation of interstitial F⁻ ions which enlarge the structure. In fact, the substitution of an eight-coordinate Ca²⁺ ion by an equally eight-coordinate Eu³⁺ or Tb³⁺ dopant ion introduces a local charge disequilibrium which can be compensated by a F⁻ additional ion in a nearby interstitial site, as depicted in Fig. 1c.

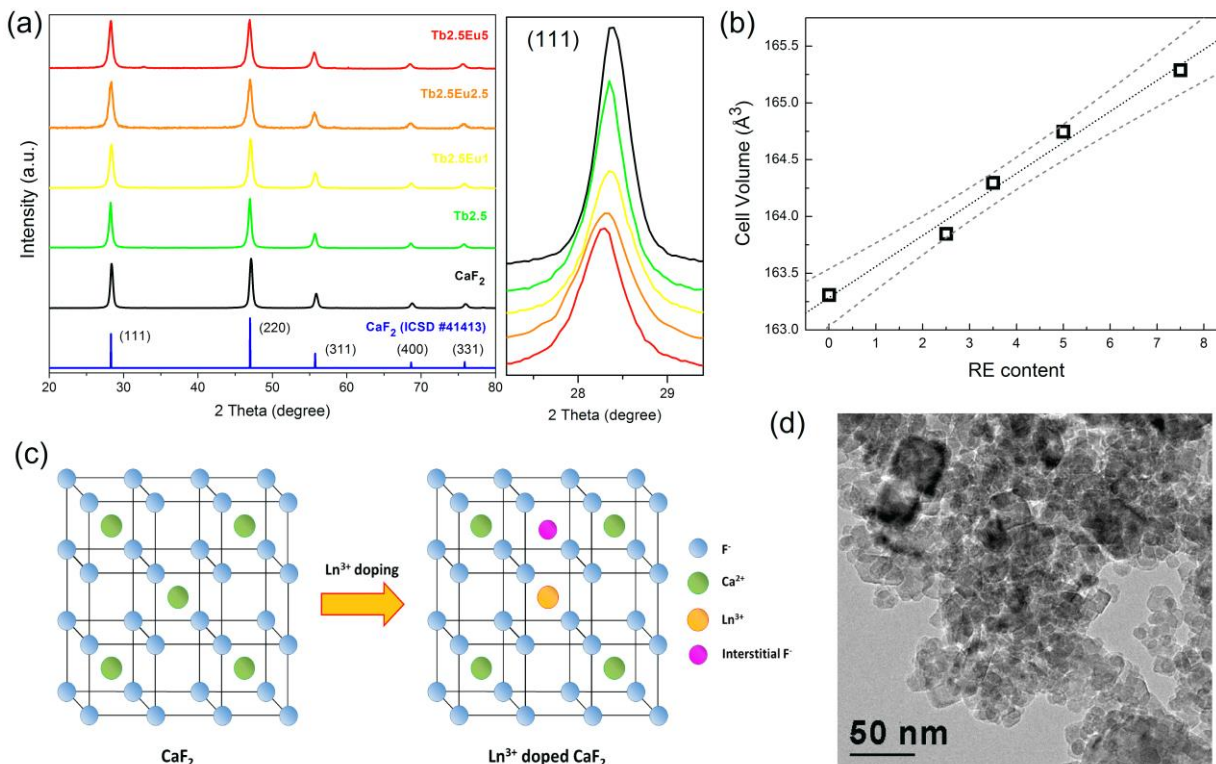


Fig. 1 (a) XRPD patterns of the samples (for the sake of clarity, sample Eu5 is not shown) and zoom of the (111) reflection. (b) Cell volume versus total lanthanide content. (c) Schematic representation of the charge compensation operated by F⁻ ion in the RE³⁺ substitution. (d) TEM image of the pure CaF₂ sample.

The small decrease of the average cell edge caused by the dopant is counteracted by the larger increase due to the interstitial fluorine, leading to the observed cell volume increase. On the other hand, the presence of this combination of substitutional and interstitial defects introduces a degree of structural disorder which is proportional to the lanthanide concentration. This explains both the gradual intensity decrease and the XRPD peak broadening with the lanthanide amount increase, as shown by the enlargement of the (111) reflections shown in Fig. 1(a).

The average crystallite size determined by the line broadening analysis of the (111) peak of the un-doped sample is about 20 nm. TEM images (see Fig. 1(d)) show particles with different shapes and a wide distribution of sizes ranging from few nanometers to some tens of nanometers.

3.2. Optical Properties

In order to investigate the Tb-Eu energy transfer process, the investigation focused on samples with a fixed donor (Tb³⁺) content (2.5 at%), while the acceptor (Eu³⁺) content was varied between 1 and 5 at%, a range in which typically no concentration quenching phenomena take place.²³ For comparison, single-doped Tb (2.5%) and Eu (5%) were also synthesized.

Fig. 2 reports a sketch of the energy level diagram for the two interacting lanthanide ions and the corresponding radiative

transitions that characterize the photoluminescence (PL) spectra discussed in the following.

The typical $^5D_0 \rightarrow ^7F_j$ ($j = 0, 1, 2, 3$ and 4) transitions of Eu³⁺ ions characterize the visible PL spectra shown in Fig. 3(a). It is well known that the intensity ratio between the $^5D_0 \rightarrow ^7F_2$ and the $^5D_0 \rightarrow ^7F_1$ transitions can be used to investigate the symmetry of the host lattice, due to the different physical nature of the two lines: the $^5D_0 \rightarrow ^7F_2$ transition (of electric dipole nature) is very sensitive to the site symmetry of the emitting Eu³⁺ ion, whereas the $^5D_0 \rightarrow ^7F_1$ one (of magnetic dipole nature) is not influenced by the local environment.²⁴ In a site without inversion symmetry the $^5D_0 \rightarrow ^7F_2$ transition prevails, while in the opposite case the $^5D_0 \rightarrow ^7F_1$ transition is the most prominent one. In the present case, the latter transition at 590 nm is predominant, indicating the high symmetry of the Eu³⁺ local environment. The spectra also show that the emission intensities increase linearly with the Eu content, as clearly visible in the inset of Fig. 3(a), confirming that no quenching concentration and back transfer processes to Tb ions take place. In fact, as previously shown,²³ concentration quenching effects usually start to take place in fluoride hosts for Eu contents of the order of 15%.

Fig. 3(b) shows the PL excitation (PLE) spectrum of the Tb2.5Eu5 sample, monitoring the emission at 590 nm, and, for comparison, those of the Tb2.5 and Eu5 samples at a detection wavelength of 545 nm (one of the most intense Tb³⁺ emission lines) and 590 nm, respectively. It is clear that the spectrum of

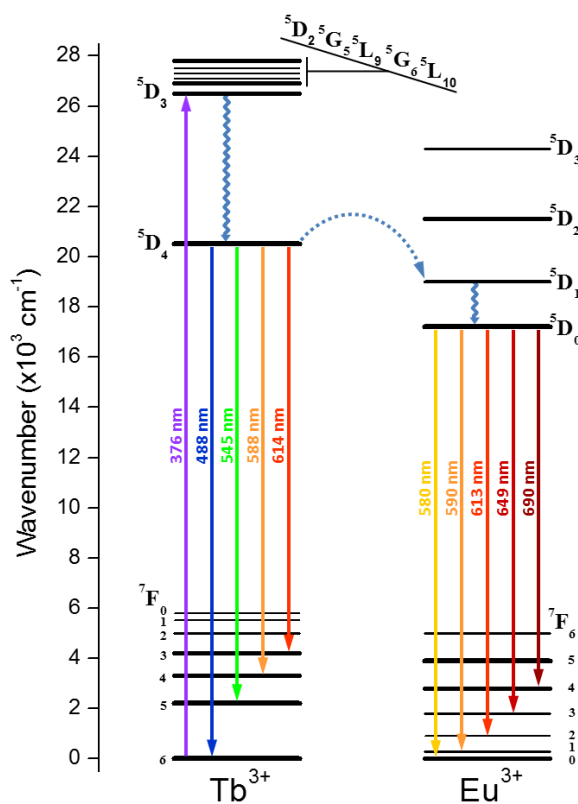


Fig. 2 Energy level diagram and related optical transition for Tb^{3+} and Eu^{3+} ions.

the codoped $\text{Tb}2.5\text{Eu}5$ sample includes all spectral features detectable for both the single doped $\text{Tb}2.5$ and $\text{Eu}5$ samples, and, in fact, the sum of the spectra of the two single doped samples perfectly matches the spectrum of the codoped system, as evidenced in Fig. S1. The presence of the Tb^{3+} absorption lines among the different photostimulation paths for the activation of the $\text{Eu}^{3+} \ ^5\text{D}_0 \rightarrow ^7\text{F}_1$ transition at 590 nm can be considered as a manifest evidence for the occurrence of an energy transfer process between Tb and Eu ions. Moreover, as expected, the intensity of the lines related to the Eu^{3+} absorption transitions increases with the Eu content, while the intensity of the Tb^{3+} ones remains constant (see Fig. S2, where PLE spectra of all of the samples is compared).

Fig. 4(a) shows how the energy transfer between Tb^{3+} and Eu^{3+} allows one to finely tune the colour emission from green to orange-red, simply selecting the suitable Tb/Eu ratio. The spectra reported therein, obtained by 376 nm sample excitation, are characterized by the typical transitions in the visible range for both Tb^{3+} and Eu^{3+} ions. The impact of the Eu^{3+} incorporation on the activation of the Tb^{3+} emission lines can be appreciated by considering the evolution of the $^5\text{D}_4 \rightarrow ^7\text{F}_5$ transition at 545 nm in the spectra of Fig. 4(a): for this line, we observe the decrease of the related intensity by increasing the acceptor content, whereas the signal of the Eu^{3+} transitions progressively enhance. This is quantitatively shown in Fig. 4(b), where the emission intensities for $\text{Tb}^{3+} \ ^5\text{D}_4 \rightarrow ^7\text{F}_5$ and Eu^{3+}

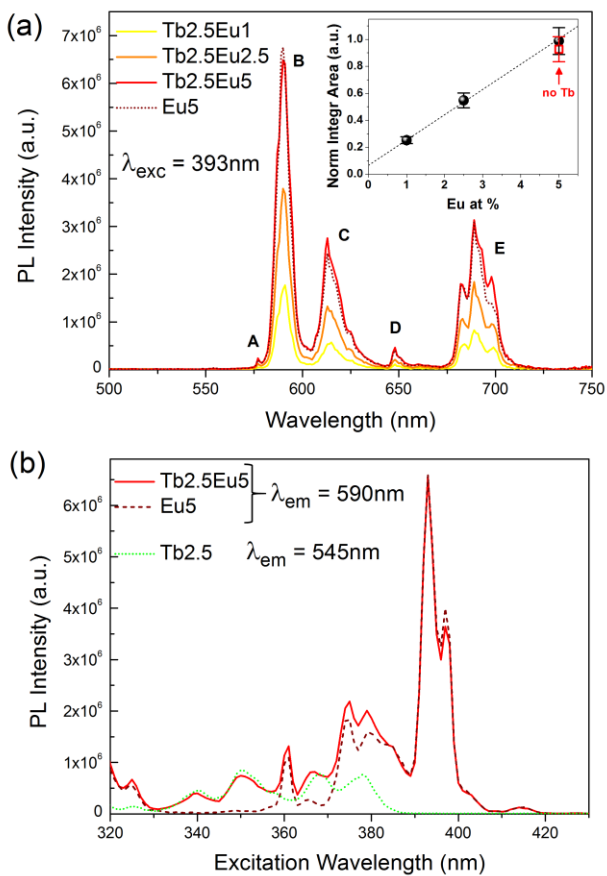


Fig. 3 (a) PL spectra of Eu and Tb codoped samples under excitation at 393 nm; the alphabetical labels denote the series of $\text{Eu}^{3+} \ ^5\text{D}_0 \rightarrow ^7\text{F}_j$ transitions, where A corresponds to $j = 0$, B to $j = 1$, C to $j = 2$, D to $j = 3$ and E to $j = 4$, respectively. Inset: trend of the overall integrated PL emission as a function of the Eu content; the red label denotes the Tb-free sample doped with 5 at.% of Eu. (b) PL excitation spectra for the emission related to the $\text{Eu}^{3+} \ ^5\text{D}_0 \rightarrow ^7\text{F}_1$ and the $\text{Tb}^{3+} \ ^5\text{D}_4 \rightarrow ^7\text{F}_5$ transitions.

$^5\text{D}_0 \rightarrow ^7\text{F}_2$ transitions are shown as a function of the Eu/Tb content ratio; this trend gives further support to the hypothesis of the occurrence of an energy transfer interaction between the two lanthanide ions. This is also corroborated by the decreasing trend of the absorptive features in the PLE spectrum for the $\text{Tb}^{3+} \ ^5\text{D}_4 \rightarrow ^7\text{F}_5$ at 545 nm when the europium content is increased, as shown in Fig. S3. The interesting possibility to tune the colour emission by controlling the Tb/Eu ratio is underlined by the CIE x,y chromaticity diagram displayed in Fig. 5.

Fig. 6(a) and 6(b) show the time-resolved PL curves recorded at 545 nm (main Tb^{3+} line) and 590 nm (main Eu^{3+} line), respectively. The non-exponential behaviour observed for the decay traces can be ascribed to the intrinsic disorder of the matrix that determines a local variation in the lanthanide environment. As previously discussed, it is well established that the substitution of Ca^{2+} by a trivalent ion is compensated by interstitial F^- ions, with possible transferring of halogen ions into octahedral interstitial sites, thus resulting in several different symmetries for the lanthanide sites. Because of the

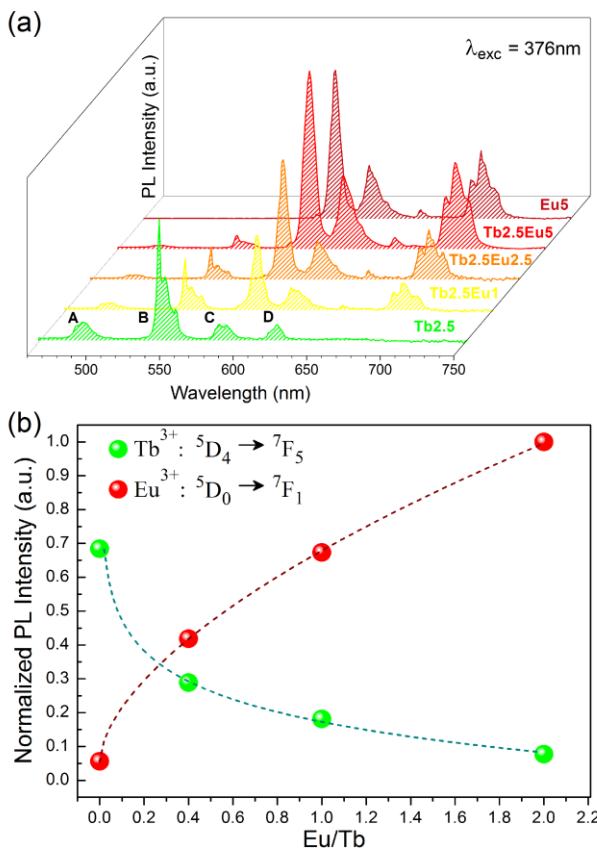


Fig. 4 (a) Evolution of the PL spectrum in the visible range under 376 nm excitation as a function of the Eu³⁺ content; the alphabetical labels denote the series of Tb³⁺ 5D₄→7F_j transition, where A corresponds to j = 6, B to j = 5, C to j = 4 and D to j = 3, respectively. (b) Trend of PL intensity as a function of Eu/Tb content ratio for Eu³⁺ 5D₀→7F₁ and the Tb³⁺ 5D₄→7F₅ radiative transitions; for all sample the Tb content was set at 2.5 at.%

non-exponential nature of the decay curves, the excited state lifetime was evaluated as an effective lifetime $\tau_{eff} = \int I(t)t dt / \int I(t) dt$ equation, where $I(t)$ represents the luminescence intensity at time t after the cutoff of the pumping light source.

The observed behaviour for the decay of the Tb PL signal shown in Fig. 6(a) is characterized by a progressive shortening of the Tb³⁺ excited state lifetime as the Eu³⁺ content increases. The reduction of the excited state lifetime from about 5 to 3 ms, as evidenced in the inset of Fig. 6(a), can be ascribed to the competitive energy transfer mechanism occurring when Eu³⁺ is present. It is worth noticing that a starting value of about 5 ms is in agreement with the typical 5D₄ excited state lifetime of Tb³⁺ ions in fluoride hosts.⁷

On the other hand, from the Eu PL decay curves in Fig. 6(b), a lifetime estimation of about 10 ms for the Eu³⁺ 5D₀ excited state is obtained, which is very long compared to the value of 5.6 ms reported by J. Labégue *et al.* for Eu doped CaF₂ nanoparticles made by a different synthesis procedure,²⁵ indicating that in the present samples the Eu³⁺ ions are in a more symmetric environment, as observed in other fluoride

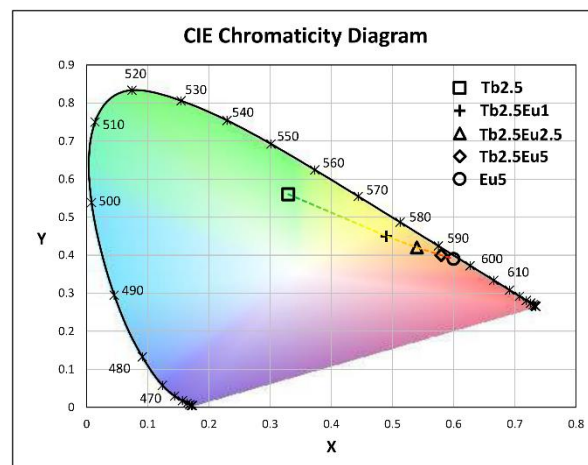


Fig. 5 CIE chromaticity diagram for the synthesized lanthanide doped samples.

hosts where similar duration were measured.²⁶ From the inset of Fig. 6(b), it can be noticed that the lifetime decreases by increasing the Eu content, as expected in virtue of the supposed enhancement of the structural disorder level pointed out by commenting XRPD data.

3.3. Energy transfer mechanism

With the aim of more thoroughly investigating the energy transfer mechanism between Tb³⁺ and Eu³⁺, the key parameters involved in the energy transfer process are detailed discussed in the following.

As a premise, we have to point out that several theoretical approaches based on the analysis of the dynamics of the fluorescence decay traces were considered in order to model the donor-acceptor interaction. We can mention the Inokuti-Hirayama model,²⁷ based on the assumption of a direct donor-acceptor energy transfer excluding donor-donor (or acceptor-acceptor) migration processes, but the simulations strongly deviates from the experimental curves probably because of some energy migration processes involved. Then, the Burshtein and Yokota-Tanimoto models have been tested.^{28,29} These models consider that the energy transfer mechanism is assisted by energy migration among donors but, depending the fits realized on a great number of parameters with no literature to draw from, the level of confidence for the obtained results is too arbitrary.

In general, we can consider that all these models are usually adopted in the context of bulky systems and not of nanosized environments, where local surface states can strongly affect the overall evolution of the fluorescence dynamics. Moreover, as reported by Rabouw *et al.*,³⁰ a random substitutional doping leads to an ensemble of donor ions with a different number of and separation from nearby acceptors, factors not considered by the above mentioned approaches.

Therefore, while reserving for the future the development of fluorescence decay models, in the following we try to spread light on the nature of the observed energy transfer mechanism by means of studies based on the evolution of the donor emission intensity.

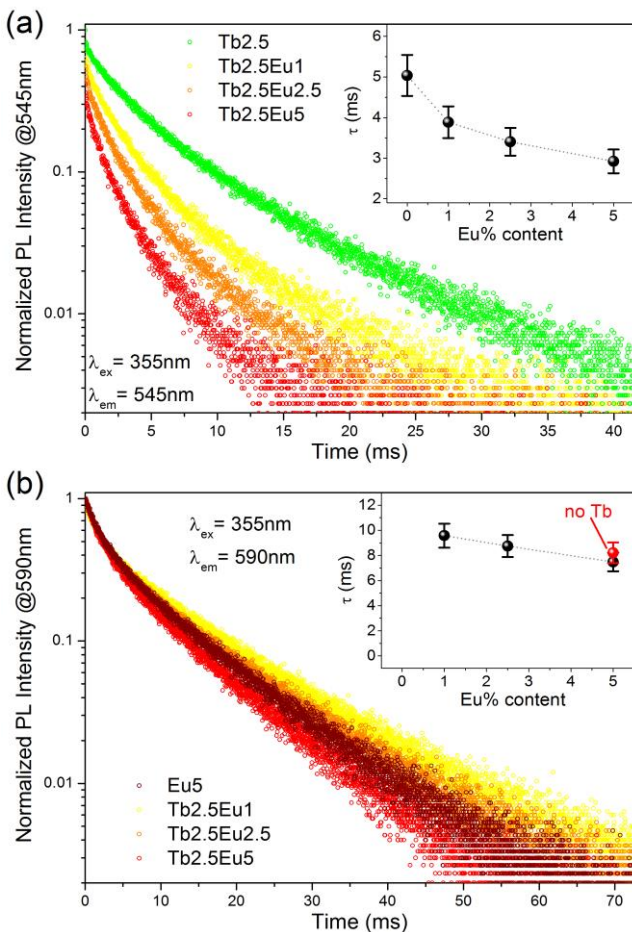


Fig. 6 PL time decay curves taken at (a) 545 nm (Tb^{3+} - $^5D_4 \rightarrow ^7F_5$ transition) and (b) 590 nm (Eu^{3+} - $^5D_0 \rightarrow ^7F_1$ transition); the excitation wavelength was set at 355 nm.

The energy-transfer efficiency η_{ET} from Tb^{3+} to Eu^{3+} can be expressed by the following relation:^{31,32}

$$\eta_{ET} = 1 - \frac{I_S}{I_{S0}} \quad (1)$$

where I_{S0} and I_S are the luminescence intensity of the sensitizer (Tb^{3+}) in absence and in presence of the activator (Eu^{3+}), respectively. In Fig. 7(a), the η_{ET} trend as a function of the Eu content is shown. The ET efficiency increases as the Eu³⁺ content grows up, reaching a maximum value of about 90% for the Tb2.5Eu5 sample.

In order to estimate the critical energy transfer distance R_C between Tb^{3+} and Eu^{3+} , the formula suggested by Blasse was used:³³

$$R_C \approx 2 \left[\frac{3V}{4\pi x_C N} \right]^{1/3} \quad (2)$$

where V is the unit cell volume, N is the number of Ca^{2+} in the CaF_2 unit cell and x_C is the critical concentration. For CaF_2 host, $V = 164 \text{ \AA}^3$, $N = 4$ and the x_C is of about 0.035 (total concentration of Tb^{3+} and Eu^{3+} at which the energy transfer efficiency is 0.5). According to the above equation, the critical energy transfer distance is estimated to be about 13 Å.

Three different mechanisms can be involved in a donor-acceptor energy transfer process: exchange interaction,

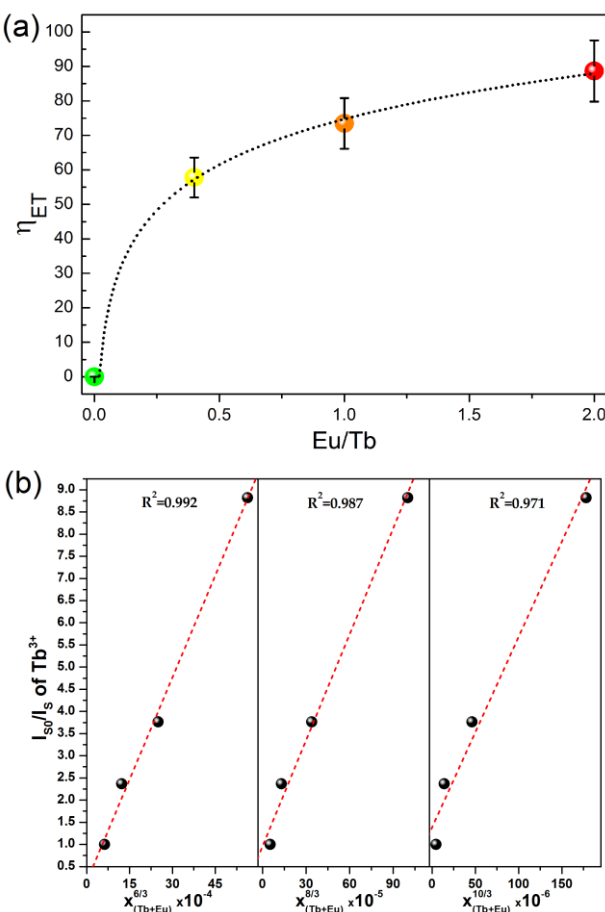


Fig. 7 (a) Trend of energy transfer efficiency η_{ET} as a function of Eu/Tb ratio; the dotted line is a guide for the eye. (b) Trend of I_{S0}/I_S on $x^n/3$ by setting $n = 6, 8$ and 10; data linear fit are represented by the dashed lines.

radiative transfer and multipole-multipole interaction. However, exchange interaction is characterized by typical values of critical distance of about 3-4 Å and can be thus excluded.³⁴ Moreover, radiative transfer can be neglected because (i) the lifetime of the Tb^{3+} emission clearly decreases as the Eu content is raised and (ii) no spectral dips occur in the PL emission spectrum of the sensitizer (Tb^{3+}) that can be linked to absorption features of the acceptor (Eu^{3+}).

Concerning the type of multipolar interaction, on the basis of Dexter's energy-transfer expressions,³⁵ and Reisfeld's approximation,³⁶ the following relation can be obtained:

$$\frac{\eta_{S0}}{\eta_S} \propto x^{n/3} \quad (3)$$

where η_{S0} and η_S are the luminescence quantum efficiencies of Tb^{3+} in the absence and presence of Eu^{3+} , respectively, x is the total concentration of the Tb^{3+} and Eu^{3+} ions, and $n = 6, 8$ and 10 correspond to dipole-dipole, dipole-quadrupole, and quadrupole-quadrupole interactions, respectively. Moreover, the value of η_{S0}/η_S can be approximately replaced by the ratio of the related luminescence intensities I_{S0}/I_S , so that the equation becomes

$$\frac{I_{S0}}{I_S} \propto x^{n/3} \quad (4)$$

As can be observed in Fig. 7(b), the good linear relationship in the I_{50}/I_S on $x^{n/3}$ plot by setting $n = 6$ proves that the dipole-dipole interaction is the predominant mechanism responsible for the energy transfer observed between Tb^{3+} and Eu^{3+} ions in calcium fluoride nanocrystals.

The energy transfer behaviour through the multipolar interaction can also be analyzed by the concentration effect of the acceptor (Eu^{3+}) on the luminescence intensity of the donor (Tb^{3+}) as reported by Van Uitert.³⁷ According to the following formula:

$$\frac{I}{I_0} = \left[1 + \beta \left(\frac{C}{C_0} \right)^{\frac{n}{3}} \right]^{-1} \quad (5)$$

where I is the intensity of the donor, I_0 the intensity without acceptor, C the concentration, C_0 the critical transfer concentration and β is a constant depending on the kind of interaction. The value of $n = 6, 8, 10$ corresponds to dipole-dipole, dipole-quadrupole, and quadrupole-quadrupole interactions, respectively. Therefore, the dominant multipolar interaction character can be estimated plotting $\log(I_0/I - 1)$ versus $\log(C)$, as reported in Fig. 8.

The experimental data can be well fit by the Van Uitert's model, where the slope of the linear fit is $n/3 = 2.2$ and as a

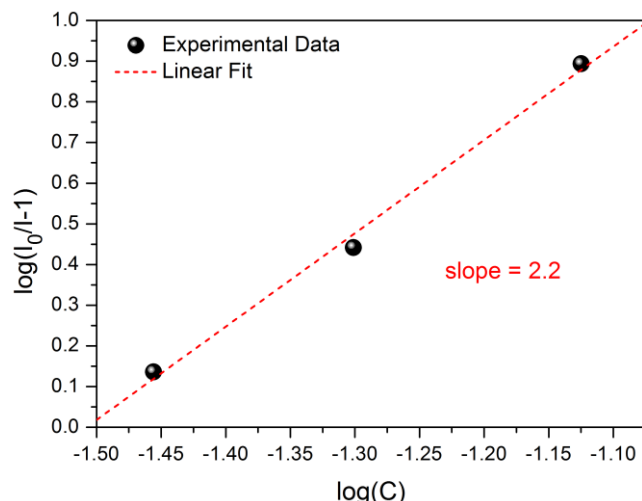


Fig. 8. Linear fitting of $\log(I_0/I - 1)$ versus $\log(C)$ based on the Van Uitert's model.

consequence $n = 6.6$, indicating the dipole-dipole interaction as the dominant in the energy transfer mechanism. This result is in agreement with the analysis carried out by means of the previous model, based on the Reisfeld's approximation of the Dexter's energy-transfer expression.

Conclusions

Inorganic nanophosphors suitable for applications in biological environments was obtained by a very facile co-precipitation method. The UV-excited emission of the water-dispersible lanthanide-doped nanoparticles can be tuned at any wavelength between red and green by a suitable choice of the Eu/Tb ratio. Energy transfer from Tb^{3+} ions to Eu^{3+} ones was

demonstrated to take place through dipole-dipole interaction. The highly efficient fluorescence activity and its long decay time makes this material an excellent candidate for bio-labelling, especially using time-resolved measurements.

Acknowledgements

Tiziano Finotto is acknowledged for technical assistance in XRD measurements.

References

- R. Kubrin, *Kona Powd. Part. J.*, 2014, **31**, 22.
- W.F. Yang, X.Y. Li, D.Z. Chi, Zhang H.J. and Liu X.G., *Nanotechnology*, 2014, **25**, 482001.
- A.H. Choi and B. Ben-Nissan, *Nanomedicine*, 2015, **10**, 2249.
- B.M. Li, Q.L. Yu and Y.X. Duan, *Critical Reviews in Biotechnology*, 2015, **35**, 82.
- M.-X. Zhao and E.-Z. Zeng, *Nanoscale Res. Lett.*, 2015, **10**, 171.
- R. Bilan, F. Fleury, I. Nabiey and A. Sukhanova, *Bioconjugate Chem.*, 2015, **26**, 609.
- W. Zheng, D. Tu, W. Huang, S. Zhou, C. Zhuo and X. Chen, *Chem. Commun.*, 2015, **51**, 4129.
- Y. Wang, A.L. Zhang, S. Shang, Z.-K. Lui and L.-Q. Chen, *Phys. Rev. B*, 2013, **88**, 024304.
- M. Pedroni, F. Piccinelli, T. Passuello, M. Giarola, G. Mariotto, S. Polizzi, M. Bettinelli and A. Speghini, *Nanoscale*, 2011, **3**, 1456.
- M. Pedroni, F. Piccinelli, T. Passuello, S. Polizzi, J. Ueda, P. Haro-González, L. Martínez Maestro, D. Jaque, J. García-Solé, M. Bettinelli, and A. Speghini, *Cryst. Growth Des.*, 2013, **13**, 4906.
- S. Sasidharan, A. Jayasree, S. Fazal, M. Koyakutty, S.V. Nair and D. Menon, *Biomater. Sci.*, 2013, **1**, 294.
- L. Song, J. Gao and J. Li, *J. Lumin.*, 2014, **151**, 18.
- J. Zhao, Y.-J. Zhu, J. Wu and F. Chen, *J. Colloids Interf.*, 2015, **440**, 39.
- J. Wang, W. Miao, Y. Li, H. Yao and Z. Li, *Mater. Lett.*, 2009, **63**, 1794.
- D. Tu, Y. Liang, R. Liu and D. Li, *J. Lumin.*, 2011, **131**, 2569.
- Z. Liu, L. Yu, Q. Wang, Y. Tao and H. Yang, *J. Lumin.*, 2011, **131**, 12.
- H. Jiu, Y. Fu, L. Zhang, Y. Sun and Y. Wang, *Opt. Mater.*, 2012, **35**, 141.
- M. Back, M. Boffelli, A. Massari, R. Marin, F. Enrichi and P. Riello, *J. Nanopart. Res.*, 2013, **15**, 1753.
- E. Moretti, L. Bellotto, M. Basile, C. Malba, F. Enrichi, A. Benedetti and S. Polizzi, *Mater. Chem. Phys.*, 2013, **143**, 445.
- X. Zhang, P. He, L. Zhou, J. Shi and M. Gong, *Mater. Res. Bull.*, 2014, **60**, 300.
- J. Zhou and Z. Xia, *J. Mater. Chem. C*, 2014, **2**, 6978.
- B. Ritter, T. Krahl, K. Rurack and E. Kemnitz, *J. Mater. Chem. C*, 2014, **2**, 8607.
- F. Wang, X. Fan, D. Pi and M. Wang, *Solid State Commun.*, 2005, **133**, 775.
- X. Chen, Y. Liu and D. Tu, in *Lanthanide-Doped Luminescent Nanomaterials From Fundamentals to Bioapplications*, ed. Editor Name(s), Springer, Berlin, edition, 2014, 5, 75-123.
- J. Labéguerie, P. Gredin, M. Mortier, G. Patriarche and A. de Kozak, *Z. Anorg. Allg. Chem.*, 2006, **632**, 1538.
- Q. Ju, Y. Liu, D. Tu, H. hu, R. Li and X. Chen, *Chem. Eur. J.*, 2011, **17**, 8549.
- M. Inokuti and F. Hirayama, *J. Chem. Phys.*, 1965, **43**, 1978.
- A. I. Burshtein, *Sov. Phys. JETP*, 1972, **35**, 882.

- 29 M. Yokota and O. Tanimoto, *J. Phys. Soc. Japan*, 1967, **22**, 779.
- 30 F.T. Rabouw, S.A. den Hartog, T. Senden and A. Meijerink. *Nature Comm.*, 2014, **5**, 3610.
- 31 P.I. Paulose, G. Jose, V. Thomas, N.V. Unnikrishnan and M.K.R. Warrier, *J. Phys. Chem. Solids*, 2003, **64**, 841.
- 32 M. Back, E. Trave, R. Marin, N. Mazzucco, D. Cristofori and P. Riello, *J. Phys. Chem. C*, 2014, **118**, 30071.
- 33 G. Blasse, *Philips Res. Rep.*, 1969, **24**, 131.
- 34 Y. Huang, H. You, G. Jia, Y. Song, Y. Zheng, M. Yang, K. Liu and N. Guo, *J. Phys. Chem. C*, 2010, **114**, 18051.
- 35 D. L. Dexter, *J. Chem. Phys.*, 1953, **21**, 836.
- 36 R. Reisfeld, in *Rare Earth, Series Structure and Bonding*, Springer Verlag, Berlin, 1973, **13**, 53.
- 37 L.G. Van Uitert, *J. Electrochem. Soc.*, 1967, **114**, 1048.